Article

Predicting Elastic Constants of Refractory Complex Concentrated Alloys Using Machine Learning Approach

Uttam Bhandari [1], Hamed Ghadimi [1], Congyan Zhang [2], Shizhong Yang [2,*] and Shengmin Guo [1]

[1] Department of Mechanical and Industrial Engineering, Louisiana State University,
     Baton Rouge, LA 70803, USA; ubhand2@lsu.edu (U.B.); hghadi1@lsu.edu (H.G.); sguo2@lsu.edu (S.G.)
[2] Department of Computer Science, Southern University and A&M College, Baton Rouge, LA 70813, USA;
     congyan.zhang@sus.edu
*   Correspondence: shizhong.yang@sus.edu

Abstract: Refractory complex concentrated alloys (RCCAs) have drawn increasing attention recently owing to their balanced mechanical properties, including excellent creep resistance, ductility, and oxidation resistance. The mechanical and thermal properties of RCCAs are directly linked with the elastic constants. However, it is time consuming and expensive to obtain the elastic constants of RCCAs with conventional trial-and-error experiments. The elastic constants of RCCAs are predicted using a combination of density functional theory simulation data and machine learning (ML) algorithms in this study. The elastic constants of several RCCAs are predicted using the random forest regressor, gradient boosting regressor (GBR), and XGBoost regression models. Based on performance metrics R-squared, mean average error and root mean square error, the GBR model was found to be most promising in predicting the elastic constant of RCCAs among the three ML models. Additionally, GBR model accuracy was verified using the other four RHEAs dataset which was never seen by the GBR model, and reasonable agreements between ML prediction and available results were found. The present findings show that the GBR model can be used to predict the elastic constant of new RHEAs more accurately without performing any expensive computational and experimental work.

Keywords: complex concentrated alloys; elastic constants; random forest regressor; gradient boosting regressor; XGBoost regression

1. Introduction

RCCAs are refractory complex concentrated alloys with complicated compositions [1]. Unlike the more restricted refractory high-entropy alloys (RHEAs), RCCAs may include less than four main elements in the composition, have multiple phases, and have small entropy configurations. Compared to typical superalloys, RCCAs have recently attracted increasing interest as a potential choice for high-temperature structural application materials. This is because the appealing qualities of RCCAs which include outstanding high-temperature strength, ductility, high melting temperature, and oxidation resistance [2–6]. The mechanical and thermodynamic properties of alloys are directly linked to their elastic constants. For example, an elastic strain of materials under different stresses depends on the elastic constant [7]. The elastic constants are also linked to essential characteristics, including bulk modulus, shear modulus, Young's modulus, Poisson's ratio, and Debye temperatures. The Voigt–Reuss–Hill (VRH) averaging approximations can be used to estimate them [8].

Several theoretical density functional theory (DFT) studies [9–14] and experimental work [15–17] are performed to obtain the elastic characteristics of RHEAs. However, understanding of elastic constants of body-centered cubic (BCC) of RCCAs is still restricted because of a lack of high-efficiency data generation methods. It is very time consuming, expensive, and complicated to synthesize and measure the elastic constants of alloys experimentally. Additionally, computational methods need many CPU hours, making them

relatively expensive for large supercells. In the literature, resonant ultrasound spectroscopy is also reported as a decent choice to measure the elastic constants of materials. However, this experimental technique has its own limitations [18]. Therefore, to accelerate the designing of RCCAs with desired properties, it is essential to adopt a time-saving and low-cost method that can efficiently explore the elastic properties of novel RCCAs. Machine learning (ML) is a reasonably easy and cost-effective tool for quickly identifying hidden patterns in a dataset. The recent trend of applying ML models in designing HEAs is promising in determining the phase formation [19–25] and predicting mechanical properties [26–28]. ML is also applied in the biomedical field to design metallic implants [29–31]. Wen et al. [32] used the ML approach to identify an AlCoCrCuFeNi HEA system with high hardness. Meanwhile, they also experimentally synthesized the alloy to validate their hardness prediction. Klimenko et al. [33] predicted the strength of AlCrNbTiVZr RHEA using a support vector ML model with experimental validation. Using a random forest model, the Kwak group [34] predicted various mechanical properties, such as tensile strength, nanoindentation hardness, and elongation of γ- TiAl alloys. Based on the studies broadly available in the literature, it is clear that the ML approach is an economical and reliable strategy to predict the properties of materials and predict the elastic constant. Consequently, utilizing a newly produced dataset, three ML models are employed in this study to estimate the elastic constants of RCCAs. Then, the predicted elastic constants of RCCAs are compared with the available reports from the first principles and experimental methods. This research demonstrates the application of the ML as a high-throughput screening tool for designing RCCAs.

2. Data Generation and ML Models

2.1. Calculation of CALPHAD and Data Generation via DFT

The database contains binary, ternary, quaternary, and quinary RCCAs having BCC structures with refractory elements of Cr, Hf, Ta, Ti, Mo, Nb, W, Re, Zr, and V. The thermocalc-2019 package with ThermoCalc's high-entropy alloy database [35] is employed to identify the RCCAs with stable BCC phases. The predicted phases by the Thermo-Calc package are under the experimental reports [36–39]. The database for RCCAs with stable BCC phases was created by computing the elastic constants of alloys using special quasi-random structure (SQS) model [40] and the MedeA 2.22 software, Materials Design, Inc., San Diego, CA, USA [41]. The possible alloy supercell structures include AB, A_3B, ABC, A_2BC, ABCD, and ABCDE, where each A, B, C, D, and E represents one of the above refractory elements. The diagrams of different SQS structures of RCCAs used in the dataset are shown in Figure 1. The number of atoms of AB, A_3B, ABC, A_2BC, ABCD, and ABCDE supercell structures is 8, 16, 36, 32, 64, and 125, respectively. To calculate the elastic constants, i.e., C_{11}, C_{12}, and C_{44} of RCCAs, the Vienna Ab initio simulation package (VASP) [42] was used, and the first-principles DFT [43,44] simulations were carried out. The generalized gradient approximation (GGA) was utilized as an exchange-correlation function to simulate many-body electronic interactions, as implemented in the Perdew–Burke–Ernzerhof (PBE) [45]. The electron-ion interactions were detailed using the projector augmented wave (PAW) model [46]. In all calculations, a 500 eV energy cutoff was employed for the plane-wave basis. The requirements for energy and force convergences in relaxation processes are set to be 10^{-5} eV/atom and 10^{-5} eV/Å, correspondingly. A smearing parameter of 0.2 eV was used in the Methfessel–Paxton method [47]. The stability of RCCAs was checked by the formation energy, $E_f = E(RCCA) - \sum_i n_i \mu_i$, where E(RCCA) is the energy of RCCA, n_i is the number of atoms of species i, and μ_i is the chemical potential of species i. The elastic constants of 370 RCCAs are computed from the DFT calculations. By utilizing strain matrix e, altering the Bravais lattice vectors R = (a, b, c) to R′ = (a′, b′, c′), a deformation of the unit cell is generated, and the elastic constants are obtained,

$$R\prime = R \begin{pmatrix} 1 + e_{xx} & \frac{1}{2}e_{xy} & \frac{1}{2}e_{xz} \\ \frac{1}{2}e_{yx} & 1 + e_{yy} & \frac{1}{2}e_{yz} \\ \frac{1}{2}e_{zx} & \frac{1}{2}e_{zy} & 1 + e_{zz} \end{pmatrix} \tag{1}$$
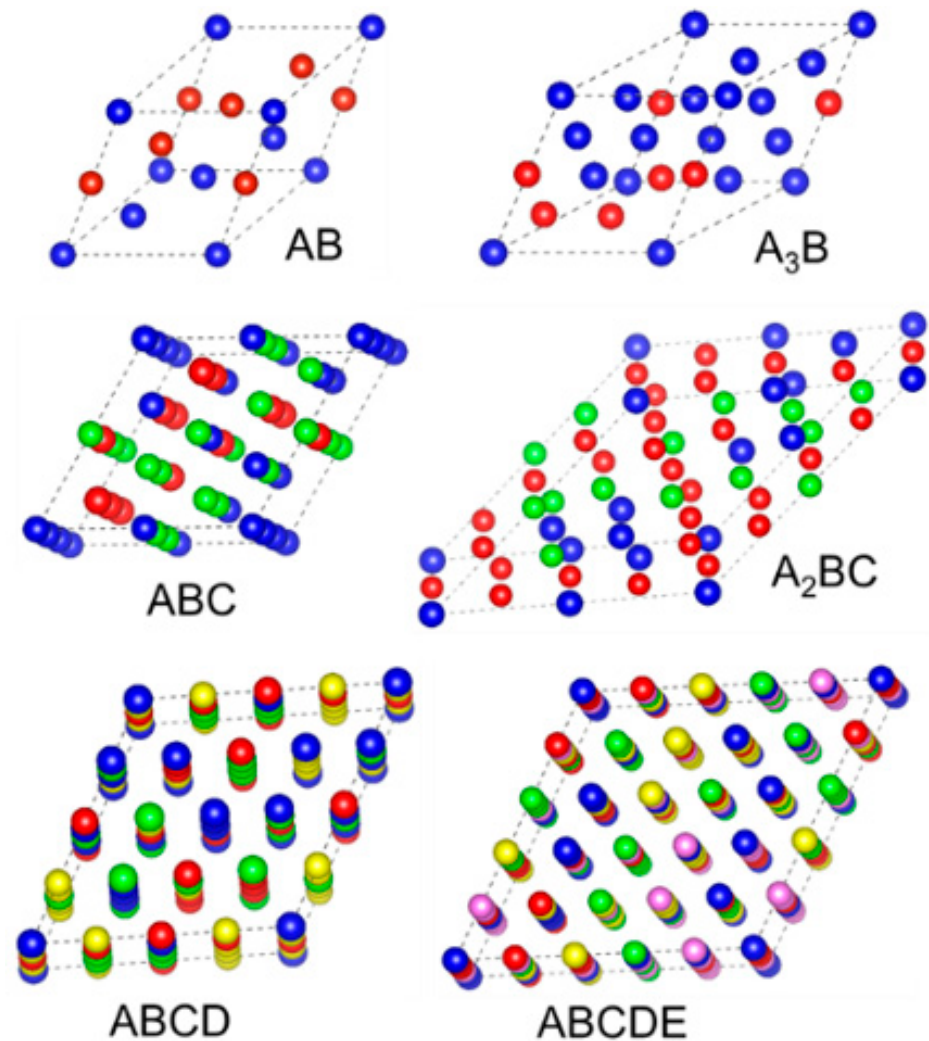
Figure 1. Different SQS models used to calculate the elastic constants of RCCAs.

Due to the deformation, total crystal energy will change. The Le Page and Saxe [48] symmetry-general approach is used for calculating elastic constants from total energy calculations,

$$U = \frac{E_{total} - E_0}{V_0} = \frac{1}{2} \sum_{i=1}^{6} \sum_{j=1}^{6} C_{ij} e_i e_j \tag{2}$$

where E_0, V_0, and C_{ij} represent the total energy of unstrained lattice, volume of the undistorted cell, and elements of the elastic constants matrix, respectively. The unit cell's symmetry can lessen the number of independent elastic constants, and it is only 3 for the cubic system, i.e., C_{11}, C_{12}, and C_{44}.

2.2. Descriptor Selection

Selecting the meaningful physical descriptors is a critical component of an ML algorithm, and the optimal choice usually depends on the target variable under investigation. It is essential to select the descriptors whose value can be predicted with any DFT computations to save computational costs. Initially, ten numeric descriptors of RCCAs and one categorical data (name of alloys) are chosen for ML models, and numeric descriptors are calculated using the Python program. The mechanical and thermal characteristics of the alloy's elemental constituents are used to calculate these descriptors. The RCCAs descriptors are entropy of mixing (ΔS_{mix}) [49], enthalpy of mixing (ΔH_{mix}) [50], the temperature of melting, average atomic radius ($\bar{r}$), average electronegativity ($\bar{\chi}$) and a dimensionless parameter omega (Ω). The Ω is defined as ΔS_{mix} divided by the ΔH_{mix} and multiplied by

alloys' average melting temperature (MT) [51]. Material properties cannot be characterized by averaging the constituent properties. Thus, it is imperative to consider the differences in properties [52]. As a result, the characteristic of these differences, i.e., atomic size difference (δ), electronegativity difference ($\Delta\chi$), and valence electron concentration (*VEC*) of RCCAs [53] are also taken into consideration. The number of descriptors used in these calculations is successfully applied in predicting the stability and properties of alloys in past studies [19–26]. For example, the Islam group [20] used 118 instances of data set with five descriptors, i.e., *VEC*, ΔS_{mix}, ΔH_{mix}, δ, and χ, to determine the phase in multi-principle element alloys. Khakurel et al. [27] used some ML models to estimate Young's modulus of CCAs. They found that *VEC*, geometrical parameter, δ, and melting temperature play essential roles in determining the modulus of CCAs. The geometrical parameter (λ), which is defined by ΔS_{mix} divided by the square of δ, has also been added as a descriptor in this work. The above-selected ten numeric descriptors are calculated using the following Equations (3)–(12), shown in Table 1. A total of 370 alloys used in the ML models are included in the form of categorical data.

Table 1. List of the mathematical formulation of descriptors used for different ML models.

Descriptors	Abbreviation	Descriptors Calculation Formula	
Entropy of mixing	Entropy	$\Delta S_{mix} = -R \sum_{i=1}^{m} a_i \ln a_i$	(3)
Enthalpy of mixing	Enthalpy	$\Delta H_{mix} = \sum_{i=1, i \neq j}^{m} 4\Delta H_{ij}^{mix} a_i a_j$	(4)
Melting temperature	MT	$T_m = \sum_{i=1}^{m} a_i (T_m)_i$	(5)
Average atomic radius	AAR	$\bar{r} = \sum_{i=1}^{n} a_i r_i$	(6)
Average electronegativity	AE	$\bar{\chi} = \sum_{i}^{n} a_i (\chi_i)$	(7)
Unitless parameter Omega	Omega	$\Omega = \dfrac{T_m \Delta S_{mix}}{|\Delta H_{mix}|}$	(8)
Atomic size difference	ASD	$\delta = 100 \times \sqrt{\sum_{i=1}^{m} a_i \left(1 - \dfrac{r_i}{\bar{r}}\right)^2 \bar{r}}$	(9)
Valence electron concentration	*VEC*	$VEC = \sum_{i=1}^{m} a_i (VEC)_i$	(10)
Electronegativity difference	ED	$\Delta\chi = \sqrt{\sum_{i}^{n} a_i (\chi_i - \bar{\chi})}$	(11)
Geometrical parameter	GP	$\lambda = \dfrac{\Delta S_{mix}}{\delta^2}$	(12)

In equations of Table 1, a_i and a_j are the atomic percentages of the ith and j^{th} element. r_i, χ_i and $(VEC)_i$ are the radius, Pauling electronegativity, and valence electron concentration of the ith element. $\bar{r}$ is averaged atomic radius, $\bar{\chi}$ is average Pauling electronegativity, T_m is the melting temperature of the element, and R is the ideal gas constant. The required data of refractory elements for calculating the descriptors are shown in Tables 2 and 3.

Table 2. The atomic radius, *VEC*, Pauling electronegativity, and Melting Temperature for refractory elements [54].

Element	Radius (Å)	VEC	Pauling Electronegativity	Melting Temperature (Kelvin)
Cr	1.249	6	1.66	2180
Hf	1.578	4	1.3	2506
Mo	1.363	6	2.16	2896
Nb	1.429	5	1.6	2750
Re	1.375	7	1.9	3459
Ta	1.43	5	1.5	3290
Ti	1.462	4	1.54	1941
V	1.316	5	1.63	2183
W	1.367	6	2.36	3695
Zr	1.603	4	1.33	2128

Table 3. The binary alloys' mixing enthalpies ΔHmix (kJ/mol) [47].

Element	Cr	Hf	Mo	Nb	Re	Ta	Ti	V	W	Zr
Cr	0	−9	0	−7	−4	−7	−7	−2	1	−12
Hf	−9	0	−4	4	−2	3	0	−2	−6	0
Mo	0	−4	0	−6	−7	−5	−4	0	0	−6
Nb	−7	4	−6	0	−26	0	2	−1	−8	4
Re	−4	−30	−7	−26	0	−24	−25	−13	−4	−35
Ta	−7	3	−5	0	−24	0	1	−1	−7	3
Ti	−7	0	−4	2	−25	1	0	−2	−6	0
V	−2	−2	0	−1	−13	−1	−2	0	−1	−4
W	1	−6	0	−8	−4	−7	−6	−1	0	−9
Zr	12	0	−6	4	−35	3	0	−4	−9	0

2.3. Machine Learning Models

There are 370 RCCAs data points from the DFT calculation. A total of 90% of data were utilized for training, and 10% were used to test and validate the results. The three ML models used in this work are random forest (RF) regressor, gradient boosting regressor (GBR), and XGBoost (XGB) through the Scikit-learn library [55], which is also used for data preparation and model assessment. The RF model is an ensemble approach consisting of many decision trees to improve prediction accuracy and reduce overfitting by averaging the trees. The samples of the training dataset may reappear in the single tree due to sampling replacement, also known as bootstrapping. GBR and XGB are multi-purpose machine learning methods that can handle both classification and regression problems. The GBR is a type of ensemble model having an iterative collection of tree models, and it is capable of learning from the previous model's mistakes. The XGBoost [56] is a powerful machine learning method that makes a quick decision by implementing boosted decision trees efficiently and effectively. After finalizing the descriptors, the 3 ML models were trained using 370 datasets of elastic constants with all calculated descriptors. The GridSearchCV function in the sklearn library was used to improve the machine learning model with a cross-validation score of 5. The adjustment of hyperparameters was essential since it impacts the overall performance of machine learning algorithms as it cross-validates the training and testing datasets. Following the searching algorithm of GridSearchCV, hyper-tuned parameters for all models were found. It was used in the model to make ML models to predict elastic constants. The root-mean-squared error (RMSE), the average coefficient of determination (R^2), and mean absolute error (MAE) are calculated for each ML model to evaluate its performance. The most satisfactory model with high performance during the training and testing phases is further used to predict the elastic constants of four experimental and simulation data. These data are entirely new to the model to predict elastic constants. The workflow of this work, as explained above, is illustrated in Figure 2.
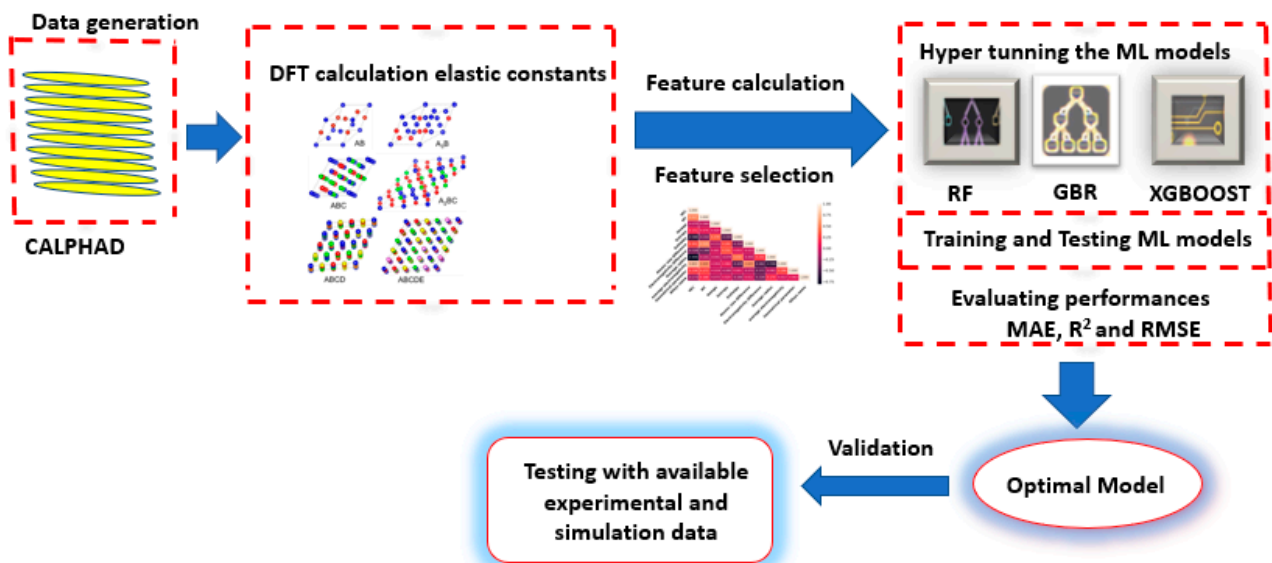
Figure 2. Graphic representation of the workflow process of the current study.

3. Results and Discussion

3.1. Feature Selection Criteria

Before applying the ML models, the Pearson correlation coefficients (p) between each pair of descriptors are calculated, and the results are shown using the triangular heatmap in Figure 3. The numeric values of p equal to 0, 1, and −1 denote no correlation, high positive correlation, and high negative correlation, respectively. The highly correlated features are likely to overfit the ML model, which is undesirable. The dark purple and light-pink colors represent highly positive and negative correlations, respectively. Two of the descriptors, i.e., average electronegativity and average radius, are strongly correlated with *VEC*, and it has been removed from the descriptor list. Since there is no substantial dependency between any two of the remaining descriptors, all metrics should be incorporated into the ML model. Therefore, the number of descriptors reduce from 11 to 9.

3.2. ML Model Performance

The elastic constant for RCCAs was predicted from the dataset by employing three ML methods: RF, GBR, and XGBoost. The dataset is randomly divided into a training and a testing set with a 9 to 1 ratio. For each approach, hyper tunning is done with a cross-validation score of 5. The different tuned hyperparameter of three ML models obtained from the Grid search method is shown in Table 4. MSA, RMSE, and R^2 are calculated for measuring the performances of the ML models using the equations below.

$$\text{MAE} = \frac{1}{n} \sum_{i=1}^{n} |y_i - \hat{y}_i| \tag{13}$$

$$\text{RMSE} = \sqrt{\frac{\sum_{i=1}^{n}(y_i - \hat{y})^2}{n}} \tag{14}$$

$$R^2 = 1 - \frac{\sum_i (y_i - \hat{y})^2}{\sum_i (y_i - \overline{y})^2} \tag{15}$$

where y_i, $\hat{y}_i$, $\overline{y}$ and n represent the DFT elastic constants, ML-predicted elastic constants, mean of all elastic constants, and sample size, respectively.
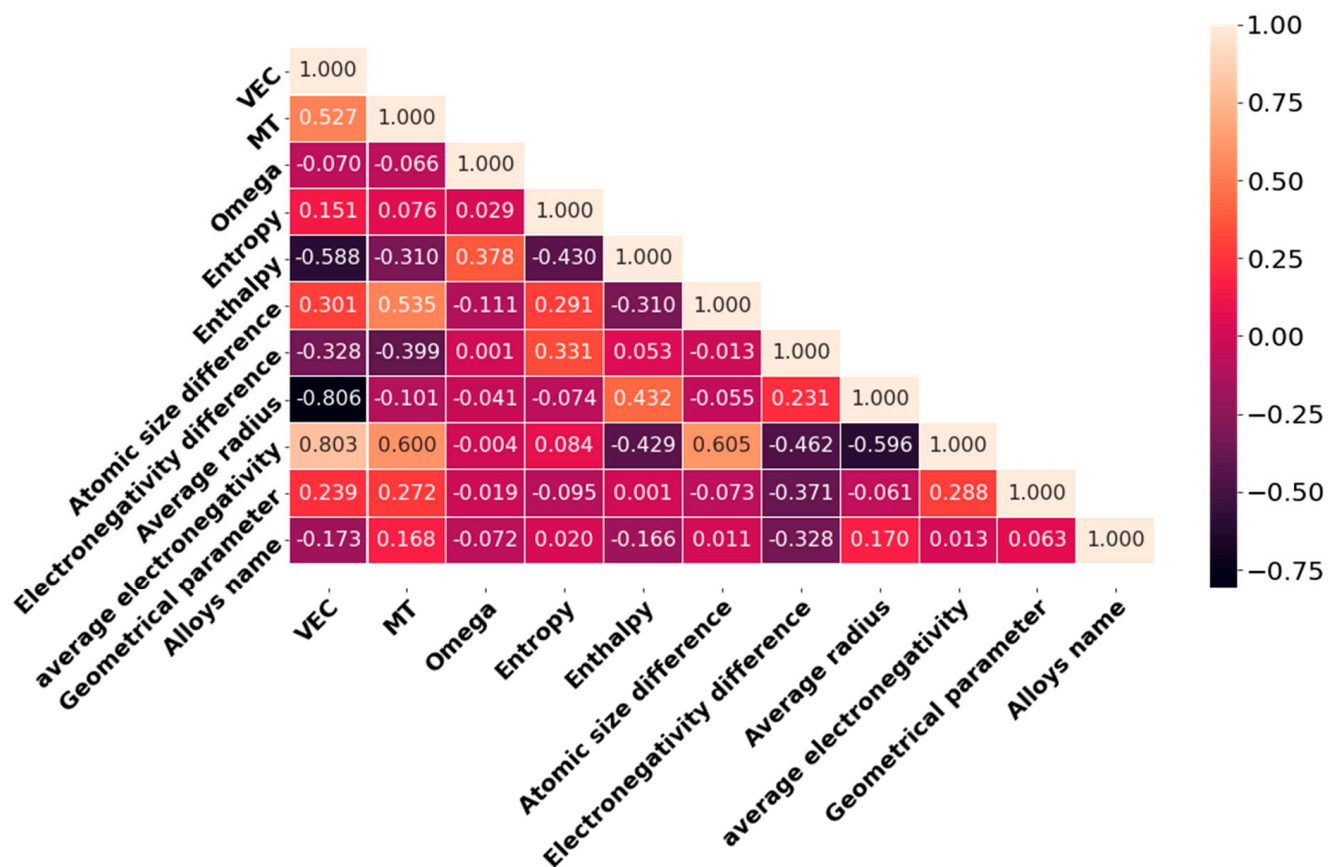
Figure 3. Lower triangular heatmap diagram of 11 descriptors of the initial datasets.

The performance metrics MAE, R^2, and RMSE of all three models are shown in Figure 4. To evaluate which model performs very well while predicting the elastic constant, MSA, R^2, and RMSE needs to be analyzed. ML model with a higher value of R^2 close to 1.0 with low MAE and RMSE will result in better performance. It is hard to distinguish which model performs well on the dataset if only R^2 is analyzed. Analyzing results from Figure 4a–c, GBR has the least MAE and RMSE with higher R^2 value than the other two ML models indicating its higher prediction accuracy of elastic constant. The R^2 value for all models ranges from 0.76–0.97 for the training and testing datasets. Similar value of R^2 was found by Trostianchyn et al. [57] while predicting the magnetic remanence of Sm-Co magnets using machine learning methods. They found the R^2 value of their ensemble ML model greater than 0.7. In this work, considering the different performance metrics of the GBR among other models, it is considered to be the optimal model.

Table 4. Tuned hyperparameter obtained from Grid Search method.

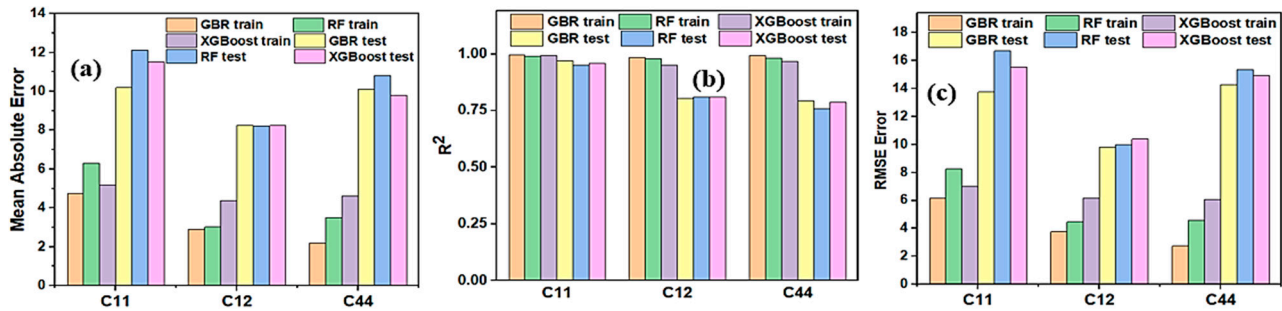| Elastic Constant	ML Models	Hyper-Tuned Hyperparameters
C_{11}	GBR	Learning rate: 0.01, max depth: 8, estimators: 900, subsample: 0.2
	RF	Max depth: 10, estimators: 1000
	XGB	Learning rate: 0.2, estimators: 100
C_{12}	GBR	Learning rate: 0.04, max depth: 4, estimators: 200, subsample: 0.7
	RF	Max depth: 10, estimators: 500
	XGBoost	Learning rate: 0.1, estimators: 100
C_{44}	GBR	Learning rate: 0.01, max depth: 6, estimators: 900, subsample: 0.3
	RF	Max depth: 10, estimators: 500
	XGBoost	Learning rate: 0.1, estimators: 100

Figure 4. (**a–c**) Represents the MAE, R^2, and RMSE of different ML models used, respectively.

The GBR model optimizes the bias while training the dataset and repeatedly trains the trees in the entire process to avoid the early paralysis of trees during the training data which results in better performance in prediction. The performance metrics of all 3 ML models are listed in Table 5. The MAE of training data of the GBR model is below 5, which means it has predicted the elastic constants of RHEAs with an average error of less than 5 GPa. Similarly, the MAE of the test data of the GBR model is less than 11 for the test dataset, which means there is not much difference in the prediction of the training and testing datasets. This manifests the testing data is not highly overfitted. The overall performances of all three models were good, which confirms that the selection of 9 descriptors fitted well for the ML models. The elastic constants predicted by the optimal GBR models versus DFT results on the training and testing datasets are illustrated in Figure 5. Most training data points (blue dots), and testing data points (dark pink diamonds) are clustered around the light blue solid diagonal line, indicating that predicted elastic constants of RCCAs predicted by the GBR ML model are consistent with the DFT calculations. Some testing data points are slightly far away from the diagonal line. It is due to the absence of sufficient data points around the relevant area. In the future, the addition of more data points will further improve the model, and data points will likely distribute evenly around the diagonal line.

3.3. Additional Testing on The Final Model

Furthermore, four experimental and simulation data of RCCAs available in the previous publications [10,17] were passed in the optimal model, i.e., GBR, to predict the elastic constants for additional testing. All the elastic constants data of four alloys is provided in Table 6 and the results are shown in Figure 6, a histogram with an error bar. The error bar denotes the deviation from the original prediction. The elastic constants predicted by the GBR ML models for TiZrVNbMo, TiZrNbMo, and TiZrVNb RHEAs are compared with the simulation conducted by Tian's group. The elastic constants predicted by the ML models are in good agreement with the SQS model calculation since the average error bar length is smaller. However, there is a slight difference between the SQS model and the ML model, which may have been caused by the number of atoms used in the model construction and the applied DFT method. The SQS structures for RHEAs of MoNbTiZr, MoNbTiVZr, and NbTiVZr consist of 128, 250, and 128 atoms, respectively. In comparison, depending on the types of RCCAs, the DFT calculation utilized in this work to build the database comprises supercells of 8, 16, 32, 36, 64, and 125 atoms. Due to inconsistency in the size of the atomic model and applied potential, there is a difference between chemical interactions of atoms in the DFT method, which results in a slight difference in elastic constants [58]. The elastic constant C_{11} predicted by the ML model for NbTaTiV matches the experimental value reported in Lee's study very well [17]. The slight difference between the ML and the experimental values of elastic constants may result from the temperature difference. The DFT models were performed at 0K, whereas the experiment was conducted at 300 K. Similar results were found while predicting the elastic constants of HEA Al0.3CoCrFeNi by Kim et al. [28]. The predicted elastic constants of HEA Al0.3CoCrFeNi deviate from the measured values from the in situ neutron-diffraction. As mentioned before, measuring elastic constants by experiment is time consuming and has its limitation. It is expected

more high throughput experimental methods will be designed to confirm the findings of the elastic constants for RHEAs MoNbTiVZr, MoNbTiZr, and NbTiVZr.

Table 5. Different metrics of the dataset using different ML models.

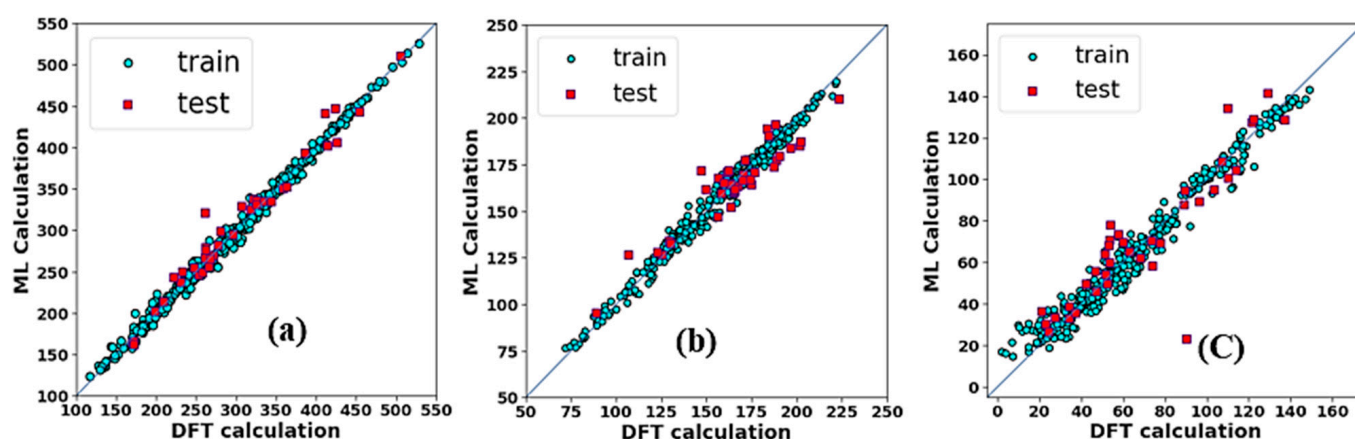| Elastic Constant	ML Models	R^2 Train	R^2 Test	MAE Train	MAE Test	RMSE Train	RMSE Test
C_{11}	GBR	0.995	0.97	4.74	10.24	6.17	13.7
	RF	0.995	0.95	6.31	12.17	8.25	16.69
	XGBoost	0.994	0.964	5.2	11.52	6.99	15.5
C_{12}	GBR	0.985	0.803	2.19	8.25	3.77	9.88
	RF	0.979	0.815	3.032	8.2	4.46	10.10
	XGBoost	0.959	0.812	4.392	8.23	6.16	10.39
C_{44}	GBR	0.994	0.787	2.20	10.38	2.67	14.45
	RF	0.981	0.761	3.58	10.86	4.62	15.4
	XGBoost	0.967	0.787	4.622	9.84	6.06	14.95

Figure 5. ML-predicted elastic constants of (**a**) C11, (**b**) C12, and (**c**) C44, as a function of DFT-predicted elastic constant during training and testing datasets.

Table 6. Elastic constants (C_{11}, C_{12}, and C_{44} are in GPa) for MoNbTiVZr, MoNbTiZr, NbTiVZr, and NbTaTiV refractory alloys experimental (exp.), and SQS.

Elastic Constants of RHEAs	MoNbTiVZr (SQS)	MoNbTiZr (SQS)	NbTiVZr (SQS)	NbTaTiV (exp)
C_{11}	209.3	203	159	196
C_{12}	123	121	114	121
C_{44}	39.12	29.6	18.5	46

SQS [10] exp. [17].

3.4. Descriptor Importance and Visualization

The Shapley Additive exPlanations (SHAP) method explains how each descriptor influences the ML by calculating the Shapley values [59]. All the dataset instances are used in the SHAP bar graph by taking the mean absolute value of every descriptor. The relevance ranking of 9 descriptors and their role in contributing to the elastic constants are displayed in Figure 7. *VEC* and MT hold the top two positions in predicting the elastic constants. From the previous findings, it is interesting to note the role of the *VEC* descriptor, which has the top position in descriptor importance in determining the crystal structure [20–25], Young's modulus [27,60,61], and hardness [62] of HEAs. The previous study has shown that *VEC* is the essential feature in determining Young's modulus of complex concentrated

alloys in their ML models [27]. Moreover, Roy et al. [63] also found that MT is an essential parameter in predicting Young's modulus of HEAs using the gradient boosting method.
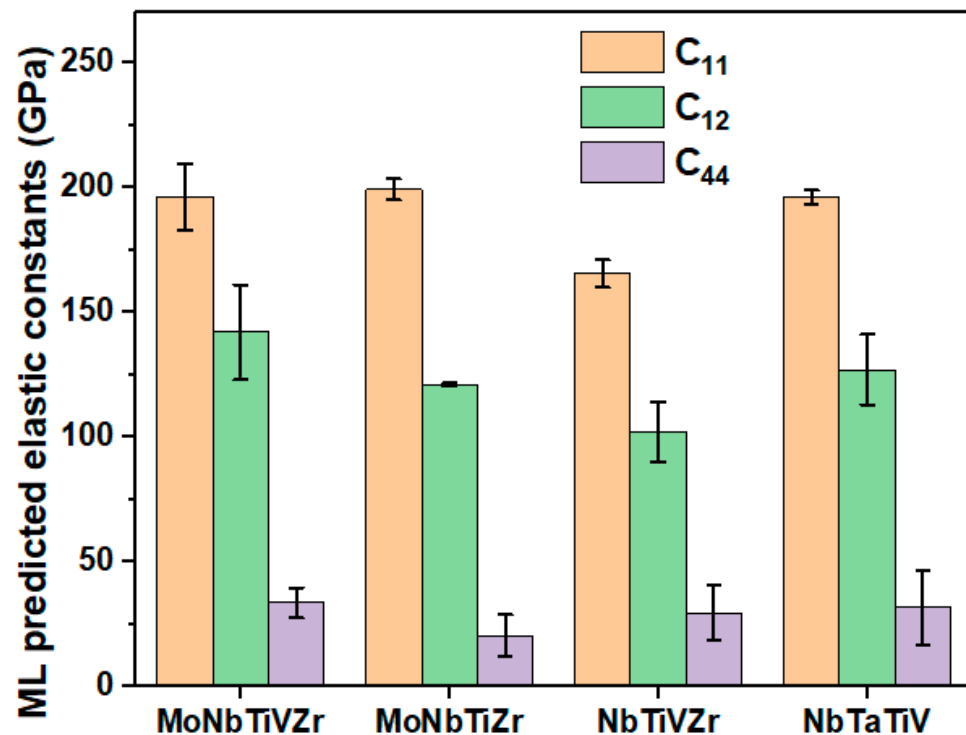

Figure 6. Elastic constants (C_{11}, C_{12}, and C_{44} are in unit GPa) for MoNbTiVZr, MoNbTiZr, NbTiVZr, and NbTaTiV refractory alloys predicted by the GBR model. The error bar shows how far the elastic constant value has deviated from its original value.

Using the SHAP value, the relevance ranking of various descriptors provides a numerical correlation between the input descriptors and target descriptors. Further details between the descriptors and elastic constant can be explored using the data visualization techniques and the concept of material. The parallel coordinate plot (PCP) of the dataset is plotted to display the correlations of the descriptor with the elastic constants, and it is shown in Figure 8. The highest value of each descriptor is shown on the top and bottom of the vertical axes, respectively. The values of alloy elastic constants are demonstrated by the three-colored bars on the right-hand side of Figure 8. The purple color represents the highest elastic constants, and yellow represents the lower elastic constant. The PCP indicates that higher *VEC*, MT, and GP values with lower omega values are favorable for developing a higher elastic constant in refractory alloys. The *VEC* value positively influences the elastic constant of RHEAs; the greater the *VEC*, the higher the elastic constant, and vice versa. This observation is quite similar to Guo et al. findings [53], which show when *VEC* is less than 6.87, the solid solution phase of the BCC is more stable due to solid strengthening caused by lattice distortion. Similar phenomena is observed from the PCP, when *VEC* lies between 5 to 6.3, the elastic constant becomes higher and it could be due to the lattice distortion. The lattice distortion is also formed when different size elements are mixed, and this mixing will force the atoms to move from their original position and result in lattice distortion. Previous work has also described the significance and importance of *VEC* in physical characteristics and phase stability in alloys [53,54,64,65]. Similar results were found by Huang et al. [66] about the *VEC*, which holds the top position in features importance while predicting the hardness of RHEAs using the RF model. They also highlight that *VEC* is important in charge transfer, which impacts RHEA strength because of lattice distortion. So far, the lattice distortion study is still in progress, and it is done by simulation only. Experimental measurement of lattice distortion in alloys is needed to get further knowledge

about the contribution of each element to the elastic properties of RHEAs. The second top descriptor is melting temperature. According to the PCA plot, RHEAs with higher melting temperatures favor the elastic constant of materials. The RHEAs consisting of elements Re, W, Ta, and Mo which have higher *VEC* and MT, have increased the alloy's elastic constant. Additional visualization using the contour plot is plotted to see the relationship between top important features *VEC* and MT with elastic constants. Figure 9a–c show the contour plot of the elastic constants of RHEAs as a function of *VEC* and MT. The original value of *VEC* and MT is normalized to get the smooth graph. The right-hand side color bar denotes the values of elastic constant in GPa. According to the contour plot, elastic constants of RHEAs increased with higher MT and *VEC* values. If MT is higher in RHEAs, with low *VEC*, then the alloy will have low elastic constants. A similar color pattern graph is obtained for all elastic constants as a function of *VEC* and MT. As a result, it is necessary to consider MT and *VEC* to get high elastic constants. The change in elastic constants with change in materials stability will help to improve the mechanical properties.
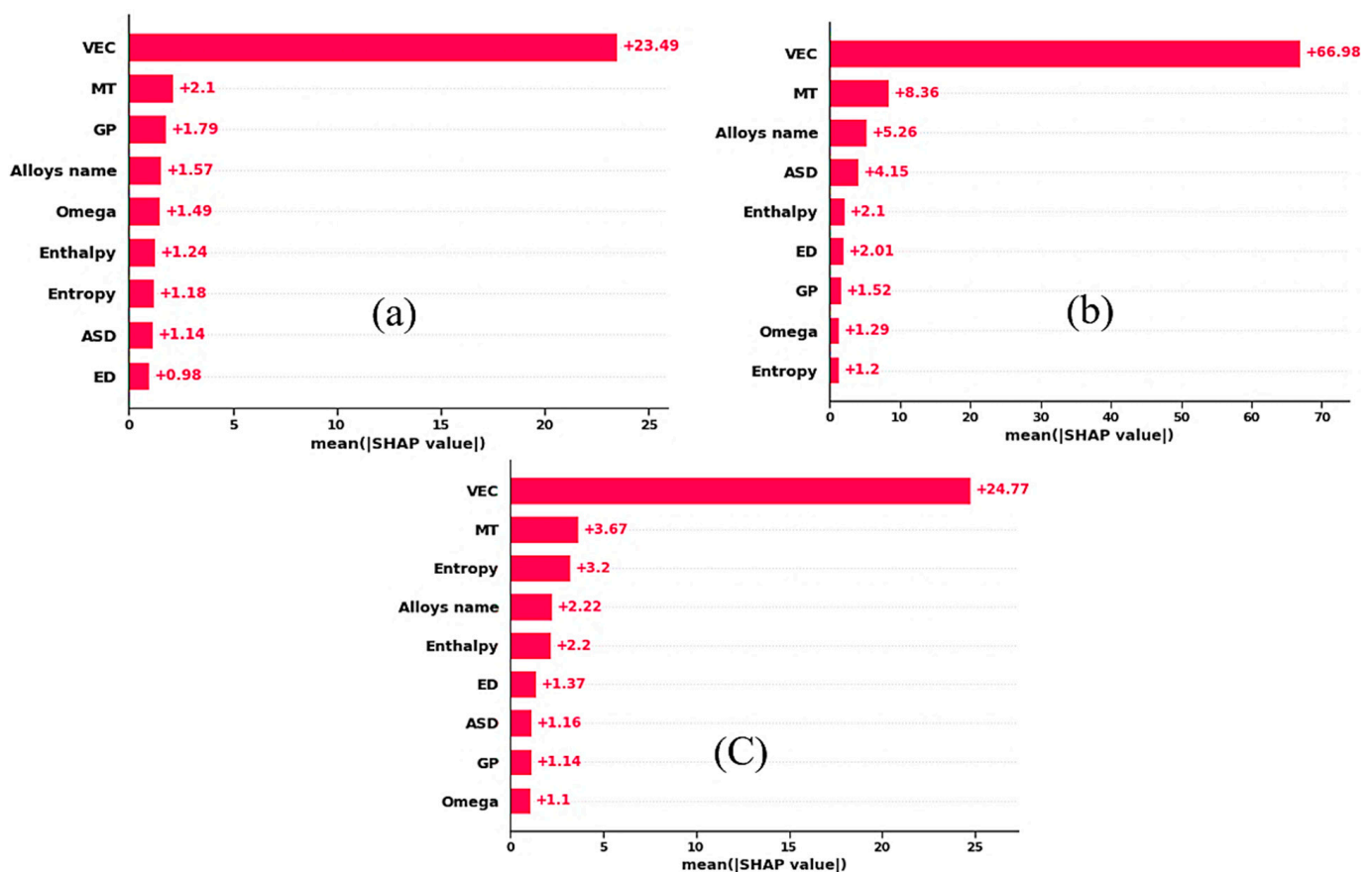

Figure 7. (**a**–**c**) Shows the SHAP value for C_{11}, C_{12}, and C_{44}, respectively.

3.5. Comparison of Current Work with Previous Work

In terms of elastic constant, Vasquez et al. [67] reported the analytical model to predict the elastic constants of RHEAs consisting of five elements Nb, Mo, Ta, W, and V alloys. In comparison, ten elements were included in the dataset in this study to give a boarder range of compositional space for alloys. Furthermore, hyper tunning of all 3 ML models is also performed, and metrics such as MSE and RMSE are calculated to find the optimal ML model capable of predicting elastic constant with higher accuracy. The dataset and model could be more beneficial to optimizing the various alloys and help in alloy design.
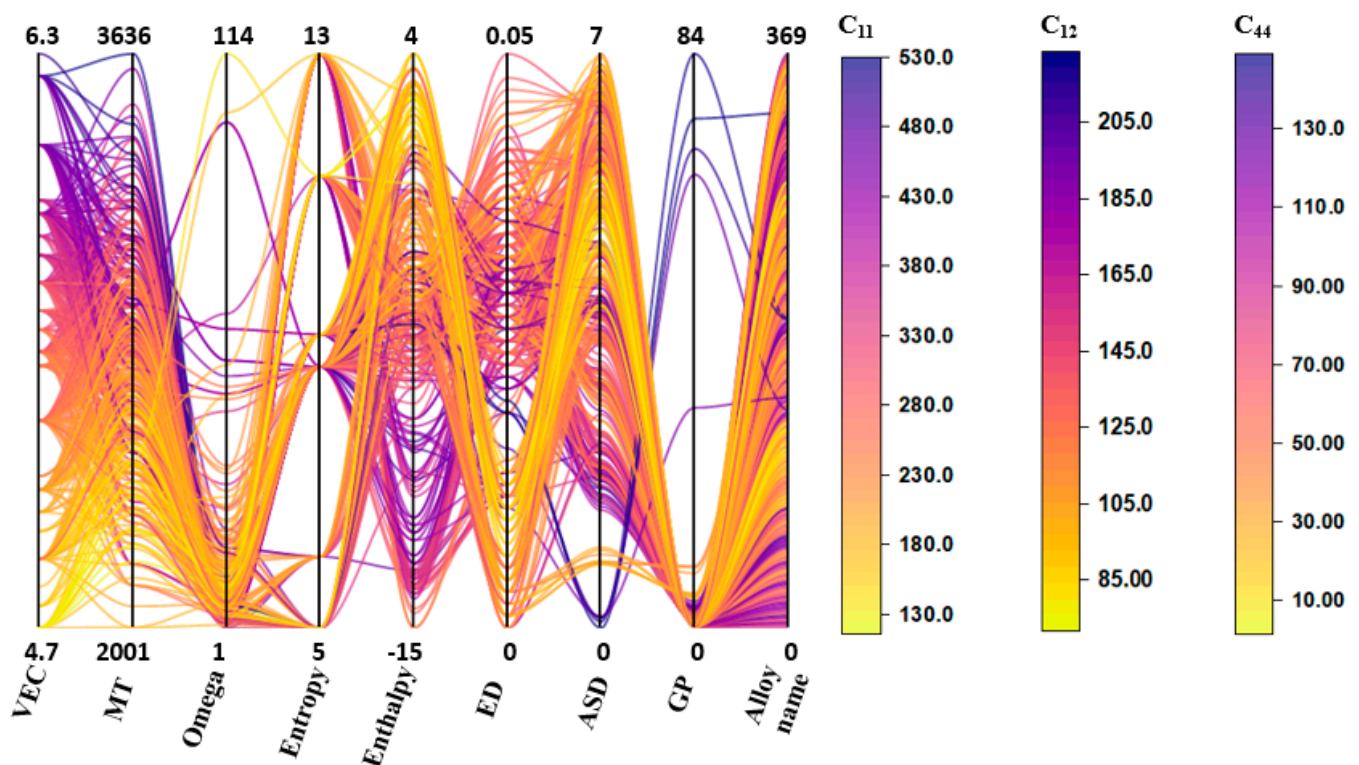
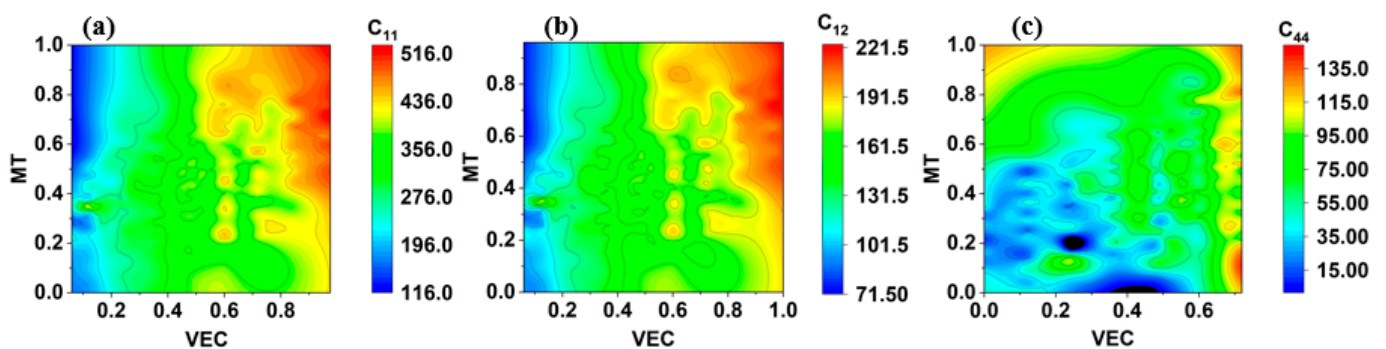**Figure 8.** Parallel coordinate plots of elastic constants (C_{11}, C_{12}, and C_{44} are in GPa) from the datasets.

Figure 9. (**a**–**c**) Represents the contour plot of elastic constants C_{11}, C_{12}, and C_{44}, respectively.

As the availability of elastic constants for RCCAs is very limited, this study demonstrates the methodology of estimating the elastic constants for RCCAs based on the ML models using a database constructed from DFT calculations. A total of 370 instances of data were created with the help of DFT computational simulations. The used database is relatively small, but as previous studies show, ML can successfully be applied to a small dataset. As an example, Islam et al. [20] also used 118 instances and five features of the multi-principal element alloys dataset, which were used to forecast the alloy's structure. Wen et al. [32] applied ML methods to the alloy system of Al-Co-Cr-Cu-Fe-Ni to find the maximum hardness with just 155 samples. Another group [68] identified the phase formation in HEAs with a small dataset by selecting low dimension descriptors. This study aimed to predict the elastic constants of RCCAs without performing any expensive DFT simulations and experimental methods, which is supposed to save time, effort, and money in designing RCCAs. It is indispensable to state that elastic constants are essential properties affecting materials' stability, strengths, and anisotropy. There is still plenty of room to optimize the compositional space of alloys. It is necessary to determine the shear strains using an atomic displacement field to evaluate the lattice distortion. The elastic constant is also one parameter for obtaining the overall influence of such local strain

changes [69]. Therefore, faster methods that are effective in exploring the compositional space of alloys for creating high-temperature and high-pressure performance materials are highly demanded. The current ML methods can acquire information from the descriptor of datasets and link the relationship between the HEAs composition and target properties, i.e., elastic constants. One achievement of this study is that if a user comes up with a new composition of an alloy, the provided Python program can predict all of the nine descriptors for the considered alloys. If the obtained information is passed into the trained ML models, the elastic constant of the given alloy will be predicted. These models may be further applied to study the compositional space of novel RCCAs, and they can be used to develop future RCCAs with desirable mechanical properties. These ML models do not consider complex phenomena such as lattice defects, dislocations, grain boundaries, slip planes, and plastic deformation in RCCAs. It is expected that more powerful models will be developed that can consider the complex phenomenon of RCCAs to make more accurate predictions of mechanical properties.

4. Conclusions

In this study, three popular ML methods, namely random forest regressor, gradient boosting regressor, and decision tree regression models, were used for predicting the elastic properties of RCCAs. The ML model consists of eight different descriptors of RCCAs. GBR performs very well as compared with the other two ML models. While predicting elastic constants C_{11}, C_{12}, and C_{44}, the R^2 value of testing data of the GBR model were 0.97, 0.803, and 0.787, respectively. The GBR model has a high R^2 value and low MAE and RMSE error than RF and XGB ML models and is promising for predicting the elastic constant of RHEAs. The elastic constants of alloys MoNbTiVZr, MoNbTiZr, NbTiVZr, and NbTaTiV predicted by the GBR model are consistent with the current simulation and experimental findings, which validate its prediction accuracy and applicability. The feature importance from SHAP and PCP plot shows that the *VEC* and MT are the most influential features affecting the elastic constants of RHEAs. The dataset created in this study using CALPHAD and DFT modeling could help scientists to construct RHEAs that can endure extreme temperatures and pressures. Compared to the computationally expensive DFT calculation and experimentally tedious trial-and-error methods for calculating the elastic constants, ML methods can be applied to predict the elastic constant of any novel refractory high-entropy alloys with very low costs, and hence helps on designing RHEAs to meet the industry demands. The GBR model is not capable of predicting the elastic constants of RHEAs at different temperatures and therefore future work should be focused on creating an ML model that can predict the elastic constants at varying temperatures.

Author Contributions: Conceptualization, U.B. and S.Y.; methodology, U.B. and C.Z. software, S.G.; validation, H.G., S.Y. and S.G.; formal analysis C.Z. and S.G.; investigation, U.B.; resources, S.Y.; data curation, C.Z.; writing—original draft preparation, U.B.; writing—review and editing, S.Y. and S.G.; visualization, H.G.; supervision, S.G.; project administration, S.Y.; funding acquisition, S.G. and S.Y. All authors have read and agreed to the published version of the manuscript.

Institutional Review Board Statement: Not applicable.

Informed Consent Statement: Not applicable.

Data Availability Statement: The dataset utilized to produce the results in this work is accessible at https://github.com/uttambhandari91/Elastic-constant-DFT-data.

Conflicts of Interest: The authors declare no conflict of interest.

References

1. Gorsse, S.; Couzinié, J.P.; Miracle, D.B. From high-entropy alloys to complex concentrated alloys. *C. R. Phys.* **2018**, *19*, 721–736. [CrossRef]
2. Gorsse, S.; Miracle, D.B.; Senkov, O.N. Mapping the world of complex concentrated alloys. *Acta Mater.* **2017**, *135*, 177–187. [CrossRef]
3. Senkov, O.N.; Gorsse, S.; Miracle, D.B. High temperature strength of refractory complex concentrated alloys. *Acta Mater.* **2019**, *175*, 394–405. [CrossRef]
4. Li, M.; Zhang, Z.; Thind, A.S.; Ren, G.; Mishra, R.; Flores, K.M. Microstructure and properties of NbVZr refractory complex concentrated alloys. *Acta Mater.* **2021**, *213*, 116919. [CrossRef]
5. Jia, Y.; Jia, Y.; Wu, S.; Ma, X.; Wang, G. Novel ultralight-weight complex concentrated alloys with high strength. *J. Mater. Sci.* **2019**, *12*, 136. [CrossRef]
6. Mishra, S.; Maiti, S.; Rai, B. Computational property predictions of Ta–Nb–Hf–Zr high entropy alloys. *Sci. Rep.* **2021**, *11*, 4815. [CrossRef]
7. Boucetta, S. Theoretical study of elastic, mechanical and thermodynamic properties of MgRh Intermetallic compound. *J. Magnes. Alloy.* **2014**, *2*, 59–63. [CrossRef]
8. Hill, R. The elastic behaviour of a crystalline aggregate. *Proc. Phys. Soc.* **1952**, *65*, 349. [CrossRef]
9. Zhang, H.; Sun, X.; Lu, S.; Dong, Z.; Ding, X.; Wang, Y.; Vitos, L. Elastic properties of AlxCrMnFeCoNi ($0 \leq x \leq 5$) high-entropy alloys from ab initio theory. *Acta Mater.* **2018**, *155*, 12–22. [CrossRef]
10. Tian, L.Y.; Wang, G.; Harris, J.S.; Irving, D.L.; Zhao, J.; Vitos, L. Alloying effect on the elastic properties of refractory high-entropy alloys. *Mater. Des.* **2017**, *114*, 243–252. [CrossRef]
11. Dirras, G.; Lilensten, L.; Djemia, P.; Laurent-Brocq, M.; Tingau, D.; Couzinié, J.P.; Perrière, L.; Chauveau, T.; Guillot, I. Elastic and plastic properties of as-cast equimolar TiHfZrTaNb high-entropy alloy. *Mater. Sci. Eng. A* **2016**, *654*, 30–38. [CrossRef]
12. Tian, F.; Varga, L.K.; Chen, N.; Shen, J.; Vitos, L. Ab initio design of elastically isotropic TiZrNbMoVx high-entropy alloys. *J. Alloys Compd.* **2014**, *599*, 19–25. [CrossRef]
13. Liao, M.; Liu, Y.; Min, L.; Lai, Z.; Han, T.; Yang, D.; Zhu, J. Alloying effect on phase stability, elastic and thermodynamic properties of Nb-Ti-V-Zr high entropy alloy. *Intermetallics* **2018**, *101*, 152–164. [CrossRef]
14. Wen, Z.; Zhao, Y.; Tian, J.; Wang, S.; Guo, Q.; Hou, H. Computation of stability, elasticity and thermodynamics in equiatomic AlCrFeNi medium-entropy alloys. *J. Mater. Sci.* **2019**, *54*, 2566–2576. [CrossRef]
15. Ye, Y.X.; Musico, B.L.; Lu, Z.Z.; Xu, L.B.; Lei, Z.F.; Keppens, V.; Xu, H.X.; Nieh, T.G. Evaluating elastic properties of a body-centered cubic NbHfZrTi high-entropy alloy—A direct comparison between experiments and ab initio calculations. *Intermetallics* **2019**, *109*, 167–173. [CrossRef]
16. Chen, L.; Zhang, X.; Wang, Y.; Hao, X.; Liu, H. Microstructure and elastic constants of AlTiVMoNb refractory high-entropy alloy coating on Ti_6Al_4V by laser cladding. *Mater. Res. Express* **2019**, *6*, 116571. [CrossRef]
17. Lee, C.; Kim, G.; Chou, Y.; Musicó, B.L.; Gao, M.C.; An, K.; Song, G.; Chou, Y.C.; Keppens, V.; Chen, W. Temperature dependence of elastic and plastic deformation behavior of a refractory high-entropy alloy. *Sci. Adv.* **2020**, *6*, 4748. [CrossRef]
18. Schwarz, R.B.; Vuorinen, J.F. Resonant ultrasound spectroscopy: Applications, current status and limitations. *J. Alloys Compd.* **2000**, *310*, 243–250. [CrossRef]
19. Pei, Z.; Yin, J.; Hawk, J.A.; Alman, D.E.; Gao, M.C. Machine-learning informed prediction of high-entropy solid solution formation: Beyond the Hume-Rothery rules. *Npj Comput. Mater.* **2020**, *6*, 50. [CrossRef]
20. Islam, N.; Huang, W.; Zhuang, H.L. Machine learning for phase selection in multi-principal Element alloys. *Comput. Mater. Sci.* **2018**, *150*, 230–235. [CrossRef]
21. Huang, W.; Martin, P.; Zhuang, H.L. Machine-learning phase prediction of high-entropy alloys. *Acta Mater.* **2019**, *169*, 225–236. [CrossRef]
22. Li, Y.; Guo, W. Machine-learning model for predicting phase formations of high-entropy alloys. *Phys. Rev. Mater.* **2019**, *3*, 095005. [CrossRef]
23. Zhang, Y.; Wen, C.; Wang, C.; Antonov, S.; Xue, D.; Bai, Y.; Su, Y. Phase prediction in high entropy alloys with a rational selection of materials descriptors and machine learning models. *Acta Mater.* **2020**, *185*, 528–539. [CrossRef]
24. Qu, N.; Chen, Y.; Lai, Z.; Liu, Y.; Zhu, J. The phase selection via machine learning in high entropy alloys. *Procedia Manuf.* **2019**, *37*, 299–305. [CrossRef]
25. Zeng, Y.; Man, M.; Bai, K.; Zhang, Y.W. Revealing high-fidelity phase selection rules for high entropy alloys: A combined CALPHAD and machine learning study. *Mater. Des.* **2021**, *202*, 109532. [CrossRef]
26. Zhang, L.; Qian, K.; Schuller, B.W.; Shibuta, Y. Prediction on Mechanical Properties of Non-Equiatomic High-Entropy Alloy by Atomistic Simulation and Machine Learning. *Metals* **2020**, *11*, 922. [CrossRef]
27. Khakurel, H.; Taufique, M.F.N.; Roy, A.; Balasubramanian, G.; Ouyang, G.; Cui, J.; Johnson, D.D.; Devanathan, R. Machine learning assisted prediction of the Young's modulus of compositionally complex alloys. *Sci. Rep.* **2021**, *11*, 17149. [CrossRef]
28. Kim, G.; Diao, H.; Lee, C.; Samaei, A.T.; Phan, T.; de Jong, M.; Jong, M.; An, K.; Ma, D.; Liaw, P.K.; et al. First-principles and machine learning predictions of elasticity in severely lattice-distorted high-entropy alloys with experimental validation. *Acta Mater.* **2019**, *181*, 124–138. [CrossRef]

29.   Izonin, I.; Tkachenko, R.; Gregus, M.; Ryvak, L.; Kulyk, V.; Chopyak, V. Hybrid Classifier via PNN-based Dimensionality Reduction Approach for Biomedical Engineering Task. *Procedia Comput. Sci.* **2021**, *191*, 230–237. [CrossRef]

30.   Izonin, I.; Tkachenko, R.; Duriagina, Z.; Shakhovska, N.; Kovtun, V.; Lotoshynska, N. Smart Web Service of Ti-Based Alloy's Quality Evaluation for Medical Implants Manufacturing. *Appl. Sci.* **2022**, *12*, 5238. [CrossRef]

31.   Izonin, I.; Tkachenko, R.; Gregus, M.; Duriagina, Z.; Shakhovska, N. PNN-SVM Approach of Ti-Based Powder's Properties Evaluation for Biomedical Implants Production. *Comput. Mater. Contin.* **2022**, *71*, 5933–5947. [CrossRef]

32.   Wen, C.; Zhang, Y.; Wang, C.; Xue, D.; Bai, Y.; Antonov, S.; Dai, L.; Lookman, T.; Su, Y. Machine learning assisted design of high entropy alloys with desired property. *Acta Mater.* **2019**, *170*, 109–117. [CrossRef]

33.   Klimenko, D.; Stepanov, N.; Li, J.; Fang, Q.; Zherebtsov, S. Machine Learning-Based Strength Prediction for Refractory High-Entropy Alloys of the Al-Cr-Nb-Ti-V-Zr System. *Materials* **2021**, *14*, 7213. [CrossRef] [PubMed]

34.   Kwak, S.; Kim, J.; Ding, H.; Xu, X.; Chen, R.; Guo, J.; Fu, H. Machine learning prediction of the mechanical properties of γ-TiAl alloys produced using random forest regression model. *J. Mater. Res. Technol.* **2022**, *18*, 520–530. [CrossRef]

35.   Andersson, J.O.; Helander, T.; Höglund, L.; Shi, P.; Sundman, B. Thermo-Calc & DICTRA, computational tools for materials science. *Calphad* **2002**, *26*, 273–312.

36.   Gao, M.C.; Carney, C.S.; Doğan, Ö.N.; Jablonksi, P.D.; Hawk, J.A.; Alman, D.E. Design of refractory high-entropy alloys. *JOM* **2015**, *67*, 2653–2669. [CrossRef]

37.   Yao, H.W.; Qiao, J.W.; Gao, M.C.; Hawk, J.A.; Ma, S.G.; Zhou, H.F.; Zhang, Y. NbTaV-(Ti, W) refractory high-entropy alloys: Experiments and modeling. *Mater. Sci. Eng. A* **2016**, *674*, 203–211. [CrossRef]

38.   Zhang, B.; Gao, M.C.; Zhang, Y.; Yang, S.; Guo, S.M. Senary refractory high entropy alloy MoNbTaTiVW. *Mater. Sci. Technol.* **2015**, *31*, 1207–1213. [CrossRef]

39.   Han, Z.D.; Luan, H.W.; Liu, X.; Chen, N.; Li, X.Y.; Shao, Y.; Yao, K.F. Microstructures and mechanical properties of TixNbMoTaW refractory high-entropy alloys. *Mater. Sci. Eng. A* **2018**, *712*, 380–385. [CrossRef]

40.   Zunger, A.; Wei, S.H.; Ferreira, L.G.; Bernard, J.E. Special quasirandom structures. *Phys. Rev. Let.* **1990**, *65*, 353. [CrossRef]

41.   MedeA® Software. Materials Exploration and Design Analysis, CA, USA. Available online: https://www.materialsdesign.com/medea-software (accessed on 22 May 2022).

42.   Kresse, G.; Furthmüller, J. Efficient iterative schemes for ab initio total-energy calculations using a plane-wave basis set. *Phys. Rev. B* **1996**, *54*, 11169. [CrossRef]

43.   Hohenberg, P.; Kohn, W. Inhomogeneous electron gas. *Phys. Rev.* **1964**, *136*, B864. [CrossRef]

44.   Kohn, W.; Sham, L.J. Self-consistent equations including exchange and correlation effects. *Phys. Rev.* **1965**, *140*, A1133–A1138. [CrossRef]

45.   Perdew, J.P.; Burke, K.; Ernzerhof, M. Generalized gradient approximation made simple. *Phys. Rev. Lett.* **1996**, *77*, 3865. [CrossRef]

46.   Blöchl, P.E. Projector augmented-wave method. *Phys. Rev. B* **1994**, *50*, 17953. [CrossRef] [PubMed]

47.   Methfessel, M.; Paxton, A.T. High-precision sampling for Brillouin-zone integration in metals. *Phys. Rev. B* **1989**, *40*, 3616. [CrossRef] [PubMed]

48.   Le Page, Y.; Saxe, P. Symmetry-general least-squares extraction of elastic coefficients from ab initio total energy calculations. *Phys. Rev. B* **2001**, *63*, 174103. [CrossRef]

49.   Zhang, Y.; Zhou, Y.J.; Lin, J.P.; Chen, G.L.; Liaw, P.K. Solid-solution phase formation rules for multi-component alloys. *Adv. Eng. Mater.* **2008**, *10*, 534–538. [CrossRef]

50.   Takeuchi, A.; Inoue, A. Classification of bulk metallic glasses by atomic size difference, heat of mixing and period of constituent elements and its application to characterization of the main alloying element. *Mater. Trans.* **2005**, *46*, 2817–2829. [CrossRef]

51.   Zhang, Y.; Zuo, T.T.; Tang, Z.; Gao, M.C.; Dahmen, K.A.; Liaw, P.K.; Lu, Z.P. Microstructures and properties of high-entropy alloys. *Prog. Mater. Sci.* **2004**, *61*, 1–93. [CrossRef]

52.   Ward, L.; Agrawal, A.; Choudhary, A.; Wolverton, C. A general-purpose machine learning framework for predicting properties of inorganic materials. *Npj Comput. Mater.* **2016**, *2*, 1–7. [CrossRef]

53.   Guo, S.; Ng, C.; Lu, J.; Liu, C.T. Effect of valence electron concentration on stability of fcc or bcc phase in high entropy alloys. *J. Appl. Phys.* **2011**, *109*, 103505. [CrossRef]

54.   Sheng, G.; Liu, C.T. Phase stability in high entropy alloys: Formation of solid-solution phase or amorphous phase. *Prog. Nat. Sci.* **2011**, *21*, 433–446.

55.   Pedregosa, F.; Varoquaux, G.; Gramfort, A.; Michel, V.; Thirion, B.; Grisel, O.; Blondel, M.; Prettenhofer, P.; Weiss, R.; Dubourg, V.; et al. Scikit-learn: Machine learning in Python. *J. Mach. Learn. Res.* **2011**, *12*, 2825–2830.

56.   Chen, T.; Guestrin, C. Xgboost: A scalable tree boosting system. In Proceedings of the 22nd ACM SIGKDD International Conference on Knowledge Discovery and Data Mining, San Francisco, CA, USA, 13–17 August 2016; pp. 785–794.

57.   Trostianchyn, A.; Izonin, I.; Tkachenko, R.; Duriahina, Z. Prediction of Magnetic Remanence of Sm-Co Magnets Using Machine Learning Algorithms. In *International Symposium on Engineering and Manufacturing 2021*; Hu, Z., Petoukhov, S., Eds.; Springer: Cham, Switzerland; London, UK, 2022.

58.   Gao, M.C.; Niu, C.; Jiang, C.; Irving, D.L. Applications of special quasi-random structures to high-entropy alloys. In *High-Entropy Alloys*; Springer: Cham, Switzerland, 2010; Chapter 10; pp. 333–368.

59.   Lundberg, S.M.; Lee, S.I. A unified approach to interpreting model predictions. In Proceedings of the Advances in Neural Information Processing Systems 30 (NIPS 2017), Long Beach, CA, USA, 4–9 December 2017; p. 30.

60. Chanda, B.; Jana, P.P.; Das, J. A tool to predict the evolution of phase and Young's modulus in high entropy alloys using artificial neural network. *Comp. Mater. Sci.* **2021**, *197*, 110619. [CrossRef]
61. Grant, M.; Kunz, M.R.; Iyer, K.; Held, L.I.; Tasdizen, T.; Aguiar, J.A.; Dholabhai, P.P. Integrating atomistic simulations and machine learning to design multiprincipal element alloys with superior elastic modulus. *J. Mater. Res.* **2022**, *37*, 1497–1512. [CrossRef]
62. Yang, C.; Ren, C.; Jia, Y.; Wang, G.; Li, M.; Lu, W. A machine learning-based alloy design system to facilitate the rational design of high entropy alloys with enhanced hardness. *Acta Mater.* **2022**, *222*, 117431. [CrossRef]
63. Roy, A.; Babuska, T.; Krick, B.; Balasubramanian, G. Machine learned feature identification for predicting phase and Young's modulus of low- medium-and high-entropy alloys. *Scr. Mater.* **2020**, *185*, 152–158. [CrossRef]
64. Poletti, M.G.; Battezzati, L. Electronic and thermodynamic criteria for the occurrence of high entropy alloys in metallic systems. *Acta Mater.* **2014**, *75*, 297–306. [CrossRef]
65. Guo, S. Phase selection rules for cast high entropy alloys: An overview. *Mater. Sci. Technol.* **2015**, *31*, 1223–1230. [CrossRef]
66. Huang, X.; Jin, C.; Zhang, C.; Zhang, H.; Fu, H. Machine learning assisted modelling and design of solid solution hardened high entropy alloys. *Mater. Des.* **2021**, *211*, 110177. [CrossRef]
67. Vazquez, G.; Singh, P.; Sauceda, D.; Couperthwaite, R.; Britt, N.; Youssef, K.; Johnson, D.D.; Arróyave, R. Efficient machine-learning model for fast assessment of elastic properties of high-entropy alloys. *Acta Mater.* **2022**, *232*, 117924. [CrossRef]
68. Dai, D.; Xu, T.; Wei, X.; Ding, G.; Xu, Y.; Zhang, J.; Zhang, H. Using machine learning and feature engineering to characterize limited material datasets of high-entropy alloys. *Comput. Mater. Sci.* **2020**, *175*, 109618. [CrossRef]
69. Ye, Y.F.; Zhang, Y.H.; He, Q.F.; Zhuang, Y.; Wang, S.; Shi, S.Q.; Hu, A.; Fan, J.; Yang, Y. Atomic-scale distorted lattice in chemically disordered equimolar complex alloys. *Acta Mater.* **2018**, *150*, 182–194. [CrossRef]